The Astrophysical Journal Letters, 995:L62 (8pp), 2025 December 20 https://doi.org/10.3847/2041-8213/ae2744

Stellar Rotation in an Old Solar Twin Using ESPRESSO/VLT Validates Gyrochronology

G. Carvalho-Silva[1,2], O. Barragán[3,4], R. D. Haywood[2,6], J. Meléndez[1], and S. A. Barnes[5]
[1] Departamento de Astronomia do IAG/USP, Universidade de São Paulo, Rua do Matão 1226, 05508-090 São Paulo, SP, Brazil
[2] Astrophysics Group, University of Exeter, Exeter EX4 2QL, UK
[3] Sub-department of Astrophysics, Department of Physics, University of Oxford, Oxford OX1 3RH, UK
[4] Department of Physics, University of Warwick, Coventry CV 4 7AL, UK
[5] Leibniz Institute for Astrophysics Potsdam (AIP), Germany
Received 2025 October 16; revised 2025 November 24; accepted 2025 December 1; published 2025 December 16

Abstract

We report the detection of rotation in the old (∼7 Gyr) solar twin HIP 73815. This result provides new insight into the validity of gyrochronology beyond the solar age, a subject of intense debate in recent years. Previous claims in the literature often relied on merged or fragmented time series or on model-dependent proxies, leading to ambiguous interpretations. Thanks to ESPRESSO's service mode, we obtained an unprecedented, single, coherent data set spanning over 80 days and covering more than two full rotation cycles of this old solar twin. We measure a rotation period of $P_{\rm GP} = 31.1^{+1.3}_{-1.1}$ days, consistent with predictions from gyrochronology, in contrast with recent studies suggesting that these relations break down past the solar age. Our result demonstrates that gyrochronology remains a reliable method for estimating stellar ages for Sun-like stars at least up to ∼7 Gyr, beyond the solar age, where its validity has been under debate. Moreover, we show that with a carefully designed ground-based observational strategy, precise and accurate rotation periods can be measured even in old stars, enabling robust age determinations for Sun-like stars and providing critical calibration for independent dating methods.

Unified Astronomy Thesaurus concepts: Stellar rotation (1629); Fundamental parameters of stars (555); Stellar ages (1581); Observational astronomy (1145); Spectroscopy (1558); Radial velocity (1332); Stellar activity (1580)

1. Introduction

Stellar ages are fundamental across all areas of astronomy, from galactic archeology and stellar evolution to placing planetary evolution and the emergence of life into context. In particular, the importance for exoplanets will only grow with upcoming facilities, such as the Terra Hunting Experiment (S. J. Thompson et al. 2016) and the Habitable Worlds Observatory (N. W. Tuchow et al. 2024).

Among the available methods for stellar age estimation (D. R. Soderblom 2010), some of the most commonly used are isochronal fitting (e.g., D. M. Nataf et al. 2024; C. Swastik et al. 2024), chemical clocks (e.g., J. Shejeelammal et al. 2024; G. Casali et al. 2025), dynamical evolution (e.g., F. Almeida-Fernandes & H. J. Rocha-Pinto 2018; M. J. Veyette & P. S. Muirhead 2018), activity evolution (e.g., P. V. Souza dos Santos et al. 2024; G. Carvalho-Silva et al. 2025), and rotational evolution (e.g., D. Lorenzo-Oliveira et al. 2019; D. Gruner et al. 2023). No single method can be universally applied, as in practice we often have suitable data for only a subset of them. A key challenge in the field is therefore to calibrate and validate these methods against each other.

Regarding age–rotation relations, early observational hints of angular-momentum evolution in solar-type stars during the main sequence motivated the development of classical models describing angular-momentum loss through magnetized stellar winds (e.g., E. N. Parker 1958; L. Mestel 1968; S. D. Kawaler 1988). They explain how stellar winds extract angular momentum from the stellar surface, leading to a progressive spin-down and a monotonic increase in the rotation period with age. Skumanich's seminal work (A. Skumanich 1972) quantified this connection between stellar rotation and age by combining rotational data from stellar associations and the Sun, establishing the empirical rotational braking law now known as the Skumanich law. This insight subsequently formed the basis of the gyrochronology technique (S. A. Barnes 2003, 2007), an age-dating method that relates stellar rotation to both mass and age, and widely used relations (e.g., E. E. Mamajek & L. A. Hillenbrand 2008; S. A. Barnes & Y.-C. Kim 2010). The calibration of gyrochronology using asteroseismic ages is expected to be one of the major scientific outcomes of the PLATO mission (H. Rauer et al. 2014).

Results from Kepler field stars suggest a contradictory picture: the Sun may be approaching a critical stage in its evolution, where it could cease to spin down. This interpretation is supported by the weakened magnetic braking (WMB) hypothesis, proposed by J. L. van Saders et al. (2016) to explain the unexpectedly rapid rotation observed in evolved solar-type stars. Subsequent studies of rotation-period data from Kepler field stars claimed that pre-Kepler spin-down models fail to reproduce the long-period Kepler stars, while models incorporating WMB succeed (T. S. Metcalfe & R. Egeland 2019; J. L. van Saders et al. 2019).

It is important to note that stellar diversity must be considered. K. Kotorashvili et al. (2023) showed that the apparent deviation from Skumanich-like spin-down in older stars does not require a dynamo mode transition. Instead, the spin evolution is better represented as an envelope of solutions. This perspective emphasizes the importance of comparing the Sun with stars of truly similar mass, radius, and composition, as the

[6] STFC Ernest Rutherford Fellow.

distribution of stellar parameters alone can account for much of the observed dispersion. Such work has been done by D. Lorenzo-Oliveira et al. (2019), where they compared the Sun with solar twins and found a smooth spin down. However, this has been questioned due to the use of the projected rotational velocity, as the inclination of the rotation axis adds uncertainties (N. Saunders et al. 2024). A similar fair-comparison approach was later adopted in D. Lorenzo-Oliveira et al. (2020), this time using time series of activity proxies. In this case, the main concern raised was the precision of the stellar age (J. Christensen-Dalsgaard 2021), especially for the location of HIP 102152 on the H-R diagram, at the edge of the main sequence.

One major limitation in advancing this field is the availability of suitable data. Detecting rotational signals requires time series with a cadence comparable to the stellar rotation period and baselines covering at least two full cycles. In addition, fair comparisons require contrasting the Sun with genuine solar twins, minimizing differences in mass and chemical composition.

In this work, we present the first analysis of a high-cadence Very Large Telescope (VLT)/ESPRESSO (F. Pepe et al. 2021) time series targeting an old, well-characterized solar twin, a star in the optimal age regime for testing gyrochronology. Owing to the state-of-the-art precision of ESPRESSO, these observations allowed us to detect very low-amplitude modulations that would otherwise remain inaccessible. This constitutes the most favorable data set obtained so far for probing rotational modulation in a true old solar twin, delivering unprecedented observational constraints on stellar spin-down at advanced ages. Our approach uses $v \sin i$ only as a physically consistent sanity check and prior upper bound, and it relies on direct rotational modulation in spectroscopic time series to measure the period. Furthermore, the target star has been extensively studied using multiple independent age-dating techniques, providing a unique benchmark against which to test gyrochronology and magnetic braking scenarios.

In this Letter, we first describe the target star HIP 73815 and review its stellar parameters and age estimates (Section 2). We then present the ESPRESSO observations (Section 3), followed by the construction of the spectroscopic time series (Section 4). In Section 5, we analyze the rotational signals using periodograms and GP modeling. We discuss the implications of our rotation-period measurement for gyrochronology in Section 6, and we summarize our conclusions in Section 7.

2. HIP 73815

HIP 73815 (Gaia DR3 1160260989536170880, HD 13360) is a bright ($V = 8.17$; I. Ramírez et al. 2012), old solar twin, with an estimated age of about 7 Gyr (L. Spina et al. 2018; M. Carlos et al. 2019; G. Martos et al. 2023; J. Shejeelammal et al. 2024). This object was chosen from a list of solar twins (L. Spina et al. 2018) and had good visibility during ESO Period 113.

Stellar parameters (Table 1), except for the stellar radius, were derived in previous works (L. A. dos Santos et al. 2016; M. Carlos et al. 2019; J. Shejeelammal et al. 2024; G. Carvalho-Silva et al. 2025) using high-resolution spectra from ESO/HARPS (M. Mayor et al. 2003) on the 3.6 m telescope, with the corresponding references listed in the table. The stellar radius was estimated through isochronal fitting with the q^2 (`qoyllur-quipu`)[7] Python package (I. Ramírez et al. 2014), using basic stellar parameters from the above-cited works as input.

Table 1
Stellar Parameters

Parameter	Value	Uncertainty	References
[Fe/H]	0.02	0.01	(1)
$T_{\rm eff}$ (K)	5790	3	(1)
$\log g$ (dex)	4.33	0.01	(1)
$v \sin i$ (km s^{-1})	1.42	0.13	(2)
$R/R_\odot$	1.16	0.02	This work
$\log R'_{\rm HK}$	−5.06	0.04	(3)
[Y/Mg]	−0.13	0.01	(4)
$A({\rm Li})_{\rm NLTE}$	0.91	0.10	(5)

References. (1) L. Spina et al. (2018); (2) L. A. dos Santos et al. (2016); (3) G. Carvalho-Silva et al. (2025); (4) J. Shejeelammal et al. (2024); (5) M. Carlos et al. (2019).

Table 2
Stellar Ages from Different Methods

Method	Age (Gyr)	Uncertainty	References
Isochrones	7.3	0.3	(1)
Chromospheric ($\log R'_{\rm HK}$)	5.7	1.1	(2)
[Y/Mg]	8.3	1.1	(3)
Lithium	7.6	0.8	(1)

References. (1) G. Martos et al. (2023); (2) G. Carvalho-Silva et al. (2025); (3) J. Shejeelammal et al. (2024).

Independent age diagnostics, including isochronal, chemical, and activity-based estimates, all indicate that HIP 73815 is older than the Sun (Table 2), yielding an uncertainty-weighted mean age of 7.3 ± 0.3 Gyr.

Below, we compute the rotation period implied by $v \sin i$ and the stellar radius, treating it solely as a conservative upper bound on the true rotation period (since $\sin i \leqslant 1$). In this work, we do not use this quantity as a direct rotation measurement; rather, it serves as a physically motivated ceiling to guide subsequent time series modeling. For stars observed away from the equator-on orientation, the true rotation period must be shorter than this value.

From the projected rotational velocity $v \sin i = (1.42 \pm 0.13)$ km s^{-1} and the stellar radius $R = 1.16\,R_\odot$, the rotation period assuming $\sin i = 1$ is

$$P_{\rm rot} = \frac{2\pi R}{v \sin i}. \quad (1)$$

With $R = 1.16 \times 6.957 \times 10^5$ km, we obtain

$$P_{\rm rot} = (3.57 \pm 0.33) \times 10^6 \text{ s} = 42 \pm 4 \text{ days}. \quad (2)$$

This value represents the maximum rotation period that would be observed if the star were seen equator-on ($i = 90°$). For lower inclinations, the true equatorial velocity is larger, and the corresponding rotation period would be shorter.

[7] https://github.com/astroChasqui/q2

3. Data

3.1. Observations

The data set consists of 23 ESPRESSO/VLT observations[8] (ESO program 113.26M0, PI: G.Carvalho-Silva) of HIP 73815 spanning $\sim$ 80 nights, obtained between 2024 May 24 and 2024 August 15. We observed in the SINGLEHR mode with 1×1 binning (HR11), delivering a resolving power of $R = 140{,}000$. Detecting rotationally modulated radial-velocity signals at the few-meters-per-second level requires sub-meters-per-second precision. To mitigate solar-like oscillations, we followed the strategy described by W. J. Chaplin et al. (2019), which quantifies how exposure times act as frequency filters on p-mode signals. Their analysis shows that the optimal integration time scales with the stellar parameters through $\nu_{\max}$, the frequency at maximum oscillation power, and that for the Sun, a $\sim$10 minute exposure averages over the dominant 3–6 minute modes, reducing their residual amplitude to the $\sim$0.1 m s^{-1} level. We therefore adopted 600 s, guided by their prescription and consistency with solar-twin properties of HIP 73815. Each exposure yielded an average signal-to-noise ratio of 182 at 550 nm and a mean radial velocity (RV) uncertainty of 30 cm s^{-1}.

Ideally, to detect rotational signals over at least two rotation cycles, we would adopt a cadence of one observation every 1–2 nights over an 80 day baseline. This strategy is sufficient to distinguish night-to-night variations. Due to weather and operational constraints, we obtained data during roughly half of this cadence within the same baseline; however, the observations were well distributed, enabling coverage of different phases and inflection points over more than two rotational cycles.

4. Time Series

We constructed time series of the RVs and spectroscopic activity indicators. Most of these quantities are derived from the cross-correlation function (CCF) profile and are directly available in the ESPRESSO spectra `.fits` headers, as they are standard outputs of the ESPRESSO pipeline.[9] From the CCF, we obtain the RV, the bisector span, the FWHM, and the contrast.

Surface inhomogeneities can arise from different phenomena and are strongly correlated with stellar activity. Activity indicators are known to be modulated by stellar rotation (D. Queloz et al. 2009), so rotational signals in the RV time series may also appear in other indicators. However, each activity proxy responds differently to stellar variability. Rotational modulation in the RVs and spectroscopic indicators can be produced by both spots and faculae in different proportions; in old Sun-like stars, faculae are generally expected to dominate (G. W. Lockwood et al. 2007; N. Meunier et al. 2010; R. D. Haywood et al. 2016; G. Ponte et al. 2023; A. Araújo et al. 2025). To complement our analysis, we derived additional activity indicators using the `ACTIN` code.

A natural question is why we do not rely on high-quality, space-based light curves, which offer uninterrupted and precise photometry. Putting aside the fact that such data are unavailable for our target, large and long-lived spots in young stars indeed produce coherent rotational modulation detectable in photometry. In contrast, older Sun-like stars exhibit only small, short-lived spots, making coherent photometric rotation signals difficult to measure (H. A. C. Giles et al. 2017; G. Ponte et al. 2023). Moreover, faculae, which dominate the RV variability in such stars, are essentially invisible in broadband optical photometry because their effects are largely compensated by spots (N. Meunier et al. 2010; R. D. Haywood et al. 2016). Their extended plage networks persist for several rotation periods, imprinting long-lived signals on RVs (e.g., R. D. Haywood et al. 2022). Spectroscopy, therefore, remains the most reliable, and perhaps the only viable, method to detect rotation periods of old Sun-like stars outside of asteroseismology.

We also constructed a time series from archival HARPS data to investigate the stellar magnetic cycle (Figure 1). The activity level appears to have been close to maximum during our observations. The last HARPS point lies about 1.5 yr before the ESPRESSO campaign, suggesting that the star may have been near the activity maximum, increasing the likelihood of active regions on its surface. This provides complementary diagnostics that strengthen the detection of rotational signals and offer insights into the origin of the observed activity modulations.

5. Rotational Signals

To identify and quantify periodicities, we computed generalized Lomb–Scargle (GLS) periodograms for the RVs and each activity indicator (S-index, bisector span, and FWHM). We searched periods in the 2–100 day range using a uniform frequency grid but restricted interpretation to $P \leqslant 0.9\,\Delta T \simeq 72$ days, given the 80 day baseline. The analysis was carried out with the `Astropy` implementation of the GLS. When measurement uncertainties were available, they were used as weights so that more precise data points contributed more strongly. We adopted the standard GLS normalization and estimated false-alarm probabilities (FAPs) from the analytical null distribution; the periodograms with the 10%, 1%, and 0.1% levels are shown in the left of Figure 2.

5.1. Periodogram Analysis

The strongest peaks are found in the S-index at $P \simeq 34.7$ days (FAP $\approx 2.4\%$) and in the FWHM at $P \simeq 33.6$ days (FAP $\approx 2.8\%$); both are consistent with rotationally modulated activity, as the value lies between that expected from the stalled hypothesis (24 days) and that inferred from the projected rotational velocity (42 days). The RVs and bisector span do not show significant signals above the adopted thresholds, but both display excess power near $\sim$15 days (RVs: $P \simeq 15.4$ days, FAP $\approx 23\%$; bisector span: $P \simeq 14.5$ days, FAP $\approx 17\%$). These features are suggestive of $P/2$ harmonics of the true rotation period. In the right panel of Figure 2, we show the phase-folded time series for the strongest peaks. The first and third, corresponding to the RV and bisector span, seem to display a periodic-like modulation.

To assess the impact of our temporal sampling, we computed the window function of the data set (bottom panel of Figure 2). It exhibits a peak near $\sim$35 days, very close to the dominant periods seen in the S-index and FWHM. This similarity indicates that sampling bias may contribute to the apparent power at those periods, and therefore, the activity-

[8] Based on data obtained from the ESO Science Archive Facility with doi:10.18727/archive/21.

[9] https://ftp.eso.org/pub/dfs/pipelines/espresso

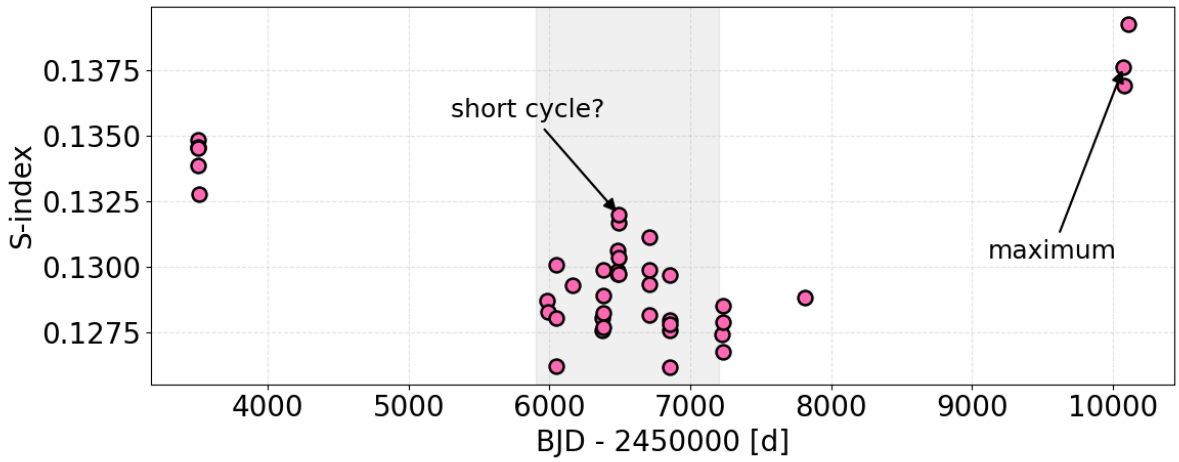

Figure 1. Time series of the *S*-index from archival HARPS data (based on observations collected at the European Southern Observatory under ESO programs 075.C-0332(A), 111.24ZQ.001, 188.C-0265(A), 188.C-0265(B), 188.C-0265(C), 188.C-0265(D), 188.C-0265(E), 188.C-0265(G), 188.C-0265(J), 188.C-0265(K), 188.C-0265(O), 188.C-0265(Q), and 188.C-0265(R)), used to investigate the stellar magnetic cycle of HIP 73815. The last point is ∼1.5 yr before the ESPRESSO observations, suggesting the star may have been near activity maximum.

related peaks must be interpreted with caution. We therefore proceed with a detailed modeling to disentangle genuine stellar variability from sampling effects.

5.2. Gaussian Process Fits to Individual Indicators

To obtain a robust estimation of the rotation signals, we modeled each proxy using a Gaussian process (GP) regression (C. E. Rasmussen & C. K. I. Williams 2005). We adopted a quasiperiodic (QP) kernel, appropriate for the behavior expected from rotational modulation by active regions (e.g., R. D. Haywood et al. 2014). We use the public code `pyaneti` (O. Barragán et al. 2019, 2022) to perform the analysis.

In `pyaneti`, the standard QP covariance kernel is defined as

$$k_{\rm QP}(t_i, t_j) = A^2 \exp\left[- \frac{\sin^2\left(\frac{\pi(t_i - t_j)}{P_{\rm GP}}\right)}{2\lambda_p^2} - \frac{(t_i - t_j)^2}{2\lambda_e^2} \right], \quad (3)$$

where A is the covariance amplitude, $P_{\rm GP}$ is the characteristic period of the process, λ_p is the inverse harmonic complexity (controlling the variability within each cycle), and λ_e is the evolutionary timescale of the correlated signal. In the stellar-activity context and timescale of days, $P_{\rm GP}$ is generally interpreted as the stellar rotation period, λ_e as the typical lifetime of active regions, and λ_p as a proxy for their longitudinal distribution.

The adopted prior ranges for the hyperparameters are summarized in Table 3, and the resulting posteriors for the dominant periodicities are reported below.

For the RVs, the GP posterior yields a characteristic period of $P_{\rm GP} = 31.6^{+1.2}_{-1.5}$ days, with an amplitude $A_0 = 3.6^{+3.6}_{-1.4}\,{\rm m\,s^{-1}}$ and hyperparameters $\lambda_e = 48^{+17}_{-20}$ days and $\lambda_p = 0.51^{+0.20}_{-0.34}$. The corresponding GP model is shown in Figure 3, where the predictive mean and its 1σ confidence interval reproduce the observed modulation with standard deviation of $\sim$45 cm s^{-1}. A similar period is found for the bisector span ($P_{\rm GP} = 30.6^{+1.5}_{-1.3}$ days).

In contrast, the FWHM also recovers a compatible period ($P_{\rm GP} \simeq 32.7$ days) but with broader posteriors and larger associated uncertainties in the hyperparameters, reflecting a less coherent signal. The *S*-index, with multiple peaks and a broad solution around $P_{\rm GP} \simeq 33.2$ days, suggests somewhat longer timescales. This behavior is consistent with the idea that different proxies are sensitive to different components of the active regions at varying heights. As pointed out in R. D. Haywood et al. (2022), at high activity levels, RV variations do not correlate well with Ca II H and K emission.

In addition to the RVs and the classical activity indicators, we also analyzed the CCF contrast. The GLS periodogram of the CCF contrast shows no peaks above our adopted significance threshold (FAP <1%). GP fits do not converge to meaningful values (covariance amplitude consistent with zero, λ_e driven to very short values, λ_p to very large values, and a multimodal period posterior without a dominant solution). We thus discard the contrast as a useful constraint in this data set.

The GP analysis highlights that different diagnostics respond differently to the underlying rotational modulation. Among the activity indicators, the bisector span and the RVs provide the most consistent constraints, both pointing to a period near 31 days ($P_{\rm GP} = 30.6$–31.6 days) with relatively well-constrained posteriors. These results suggest that both diagnostics are tracing the same physical signal, likely associated with the rotational modulation of spots and plages, which induces correlated variations in line asymmetries and RVs. The QP variations in amplitude in Figure 3, which at certain epochs appear to reinforce each other, suggest the coexistence of these two dominant active regions.

We note that subtle differences in the retrieved periods across indicators could, in principle, reflect the influence of surface differential rotation if active regions at different latitudes and heights rotate at slightly different rates. However, this is unlikely, as photometry in Sun-like stars indicates that the evolution and finite lifetimes of active regions generally dominate over differential-rotation effects in shaping the observed QP variability (e.g., S. Aigrain et al. 2015).

From a data-analysis perspective, the hyperparameters λ_e and λ_p do not necessarily correspond to different physical regimes. Relatively large values of these parameters can also arise in time series with higher white-noise levels: when random noise dominates over coherent variability, the GP tends to

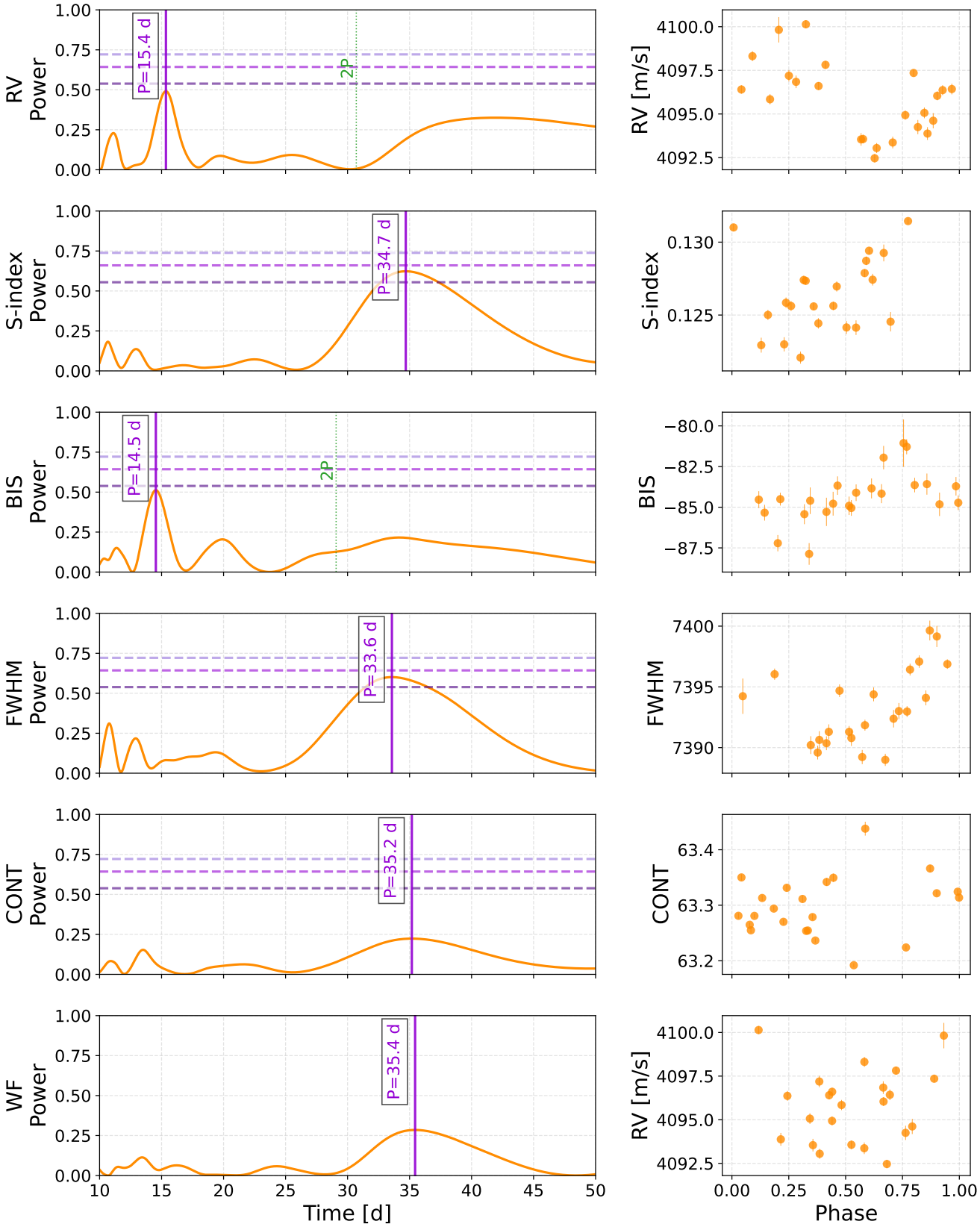

Figure 2. Left: GLS periodograms of the RVs and activity indicators (*S*-index, BIS, FWHM, and contrast), plus the window function. Horizontal dashed lines mark the false-alarm probability (FAP) levels of 10%, 1%, and 0.1%. Vertical solid and dotted lines indicate the highest peak and twice the highest peak (2P), respectively. Right: corresponding phase-folded time series at the periods of the strongest peaks.

infer longer evolutionary timescales and smoother intracycle structures, effectively mimicking a more coherent process. Such behavior may contribute to the apparent spread in the hyperparameters among indicators that are tracing related stellar signals (see the appendix of O. Barragán et al. 2023 for a detailed discussion).

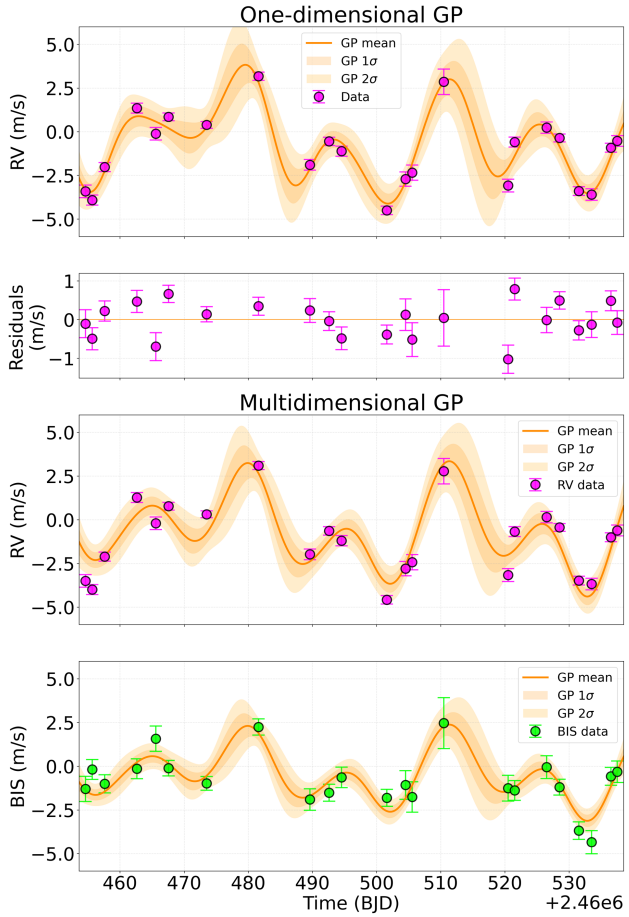

Figure 3. Time series of HIP 73815 modeled with one- and multidimensional Gaussian process (GP) regressions. Top panels: one-dimensional GP fit to the RVs and residuals. Bottom panels: joint GP fit to the RV (magenta circles) and BIS (green circles) series, showing the GP predictive mean (orange), 1σ and 2σ confidence interval (shaded), and data points with error bars. The multidimensional model highlights the consistent ∼31 day periodicity across both indicators.

Table 3
GP Hyperparameters for the RV, BIS, FWHM, and *S*-index Analyses

Parameter	Prior	RV	BIS	FWHM	*S*-index
A_0 (m s^{-1})	U[0, 5]	$3.6^{+3.6}_{-1.4}$	$2.1^{+1.5}_{-7.2}$	$4.4^{+3.4}_{-1.6}$	$3.0^{+2.9}_{-1.8}$
λ_e (days)	U[20, 80]	48^{+17}_{-20}	58^{+15}_{-20}	52^{+20}_{-21}	51^{+20}_{-22}
λ_p	U[0.001, 2.0]	$0.51^{+0.20}_{-0.34}$	$0.46^{+0.30}_{-0.15}$	$0.81^{+0.73}_{-0.49}$	$1.26^{+0.52}_{-0.67}$
$P_{\rm GP}$ (days)	U[20, 40]	$31.6^{+1.2}_{-1.5}$	$30.6^{+1.5}_{-1.3}$	$32.7^{+3.2}_{-2.6}$	$33.2^{+4.3}_{-5.4}$

Note. Priors are denoted by U (uniform). Reported values are the medians and 68% (1σ) credible intervals, with uncertainties rounded to two significant digits.

5.3. Multidimensional Gaussian Process Regression

From modeling each indicator individually, we find that the bisector span is the most reliable activity proxy, in excellent agreement with the RVs, while the CCF FWHM and *S*-index provide complementary but less tightly constrained information. The CCF contrast, however, carries insufficient signal to inform the rotation analysis.

To improve the robustness of the inferred stellar rotation period, we also performed a multidimensional GP regression (V. Rajpaul et al. 2015; O. Barragán et al. 2022) in which the RVs and activity indicators were modeled simultaneously with a common QP kernel, i.e., assumed to be described by a linear combination of the same latent GP and its time derivative. In this case, both the RVs and bisector span trace the line-profile displacements induced by active regions and are therefore described only by the latent process $G(t)$, without the derivative term $\dot{G}(t)$. Accordingly, the model takes the form $\Delta\mathrm{RV} = A\,G(t)$ and $\Delta\mathrm{BIS} = B\,G(t)$. Thus, in the implementation, the derivative amplitude component is set to zero for both rotation proxies.

Under this assumption, a multidimensional GP regression of two or more stellar time series should provide more precise and robust estimates of the stellar signal timescales, particularly the rotational period. The RVs and bisector span in the joint GP analysis reinforces the ∼31 day periodicity ($P_{\rm GP} = 31.1^{+1.1}_{-1.3}$ days), as shown in the lower panels of Figure 3, in excellent agreement with the individual fits. Including the FWHM and *S*-index shifts the solution slightly toward longer periods, around 32–33 days, consistent with the broader posteriors found for these indicators when modeled separately. The resulting combined posteriors provide a more precise constraint on the stellar rotation period while also capturing the sensitivity of different proxies to manifestations of stellar activity.

Table 4
GP Hyperparameters for the Joint BIS+RV Analysis

Parameter	Prior	BIS+RV
A_0 (m s^{-1})	U[0, 0.03]	$4.6^{+5.3}_{-2.1}$
A_1 (RV time derivative)	F[0]	…
A_2 (m s^{-1})	U[0, 0.02]	$3.3^{+3.8}_{-1.4}$
A_3 (BIS time derivative)	F[0]	…
λ_e (days)	U[25, 80]	60^{+14}_{-18}
λ_p	U[0.001, 2.0]	$0.60^{+0.40}_{-0.21}$
$P_{\rm GP}$ (days)	U[25, 40]	$31.1^{+1.3}_{-1.1}$

Note. Multidimensional GP fit including RV and BIS. A_1 corresponds to the BIS amplitude, and A_3 corresponds to the RV amplitude. Priors are denoted by U (uniform) and F (fixed). Reported values are the medians and 68% credible intervals, with uncertainties.

The priors adopted for the GP hyperparameters (in Table 4) were chosen based on the sampling properties of the data set, the location of the dominant peaks in the GLS periodograms, and the expected range of rotational periods. In particular, the upper bound on the period prior ($P_{\rm max}$) was set by the rotation period implied by $v \sin i$, as it informs the prior ceiling, not the period estimate; the data constrain $P_{\rm rot}$, while the lower bound ($P_{\rm min}$) was motivated by the WMB hypothesis. This strategy ensures that the GP search space encompasses both the observational constraints from the time series and the physically plausible limits from stellar rotation theory. We adopted positive priors for the amplitudes of RV and CCF Bisector span (BIS), since they are positively correlated. This convention breaks the sign degeneracy of the solution, preventing the posteriors from collapsing near zero.

5.4. Final Rotation Period

In summary, with the GP analyses, we consistently identify a periodicity near 31 days, most clearly seen in the RVs ($31.6^{+1.2}_{-1.5}$ days) and bisector span ($30.6^{+1.5}_{-1.3}$ days). Slightly longer values are inferred from the FWHM ($32.7^{+3.2}_{-2.6}$ days) and the *S*-index ($33.2^{+4.3}_{-5.4}$ days), while the CCF contrast fails to yield meaningful constraints.

We consider the RVs and bisector span as the most robust diagnostics, with the multidimensional GP fit shown in Figure 3 providing the most precise constraint: $P_{GP} = 31.1^{+1.1}_{-1.3}$ days. Overall, we conclude that the stellar rotation period of HIP 73815 is most robustly constrained to 30–32 days, with the joint BIS+RV GP solution providing the most reliable and precise estimate.

6. Implications for Gyrochronology

Solar twins with measured rotation periods are rare, but they constitute essential benchmarks for testing stellar spin-down models. The most notable cases include 18 Sco (G. F. de Mello & L. da Silva 1997; M. Bazot et al. 2011), HIP 102152 (T. R. Monroe et al. 2013), the oldest known solar twin analyzed by D. Lorenzo-Oliveira et al. (2020), and HIP 11915 (Y. Netto et al. 2021). To our knowledge, our target is the second well-characterized solar twin for which a direct rotation measurement has been obtained, older than the Sun but the first clearly still on the main sequence. This unique ESPRESSO data set provides unprecedented sensitivity to low-amplitude signals and allows for a critical comparison with previous age-dating methods applied to this star.

To compare our results with different gyrochronology models, we applied a minimization procedure to select the most reliable stellar age among the four independent estimates listed in Table 1. Each method was weighted by the inverse of its squared uncertainty, minimizing the dispersion across all age indicators. The weighted age is 7.3 ± 0.3 Gyr; in practice, it is identical to the isochronal age. In Figure 4, we present a zoomed-in view of age-rotation diagram on the older region where the Sun, HIP 102152 and HIP 73815 (this work) lie.

Using the color $B - V = 0.663 \pm 0.006$ (I. Ramírez et al. 2012) and the rotation period obtained from the joint GP analysis ($P_{rot} = 31.1^{+1.3}_{-1.1}$ days), the gyrochronology relation (S. A. Barnes & Y.-C. Kim 2010) yields an age of $t = 5.8 \pm 1.1$ Gyr. This rotation-based age is in agreement with expectations for a solar twin older than the Sun and confirms that the measured rotation period is physically plausible. It also agrees with the other methods, indicating that the star is on the main sequence and older than the Sun. The comparison with other prescriptions (e.g., WMB scenarios) will determine whether such formulations predict significant deviations at these ages.

Our result suggests that gyrochronology can indeed be extended beyond the solar age, but confirmation requires verifying whether the same rotational spin-down behavior is consistently observed in other Sun-like stars. Such stars are particularly valuable benchmarks because they offer more precise ages compared to single stars of other spectral types, as precise line-by-line analyses could be performed, yielding precise stellar parameters (e.g., J. Meléndez et al. 2014; P. E. Nissen 2015).

A central issue under debate, especially when comparing solar-type stars (rather than solar twins) to the Sun, is how rotational evolution diverges among stars, that is, how fundamental stellar parameters shape angular-momentum loss. It is necessary to recognize that stellar evolution unfolds in a multidimensional parameter space. In gyrochronology studies, mass (or effective temperature), age, and rotation are often emphasized, but other parameters, such as stellar composition, may play an equally fundamental role. Large surveys have revealed striking correlations among stellar properties, yet relatively little effort has been devoted to assessing how stellar

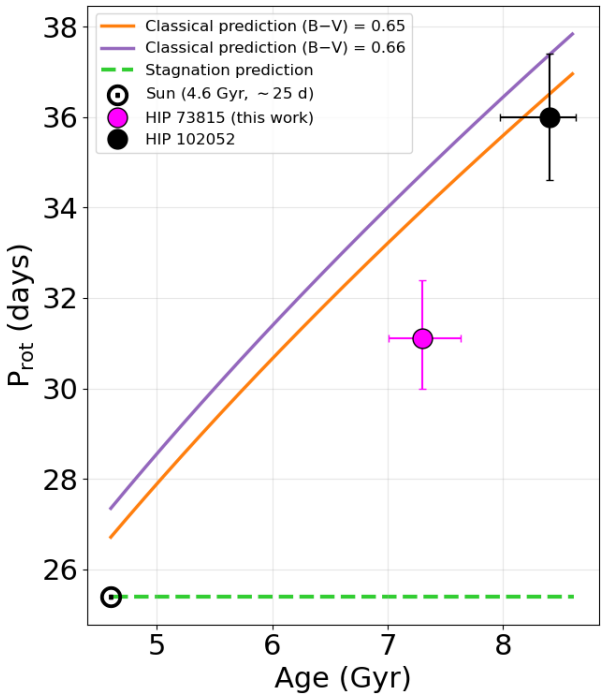

Figure 4. Rotation–age plane comparing HIP 73815 (magenta circle) and HIP 102150 (D. Lorenzo-Oliveira et al. 2019, black circle) with gyrochronology relations of S. A. Barnes & Y.-C. Kim (2010) for $B - V = 0.65$ and $B - V = 0.66$, shown as orange and purple solid lines, respectively, and with the WMB (stagnation) prediction shown as a dashed green line. The position of the Sun is also indicated for reference. HIP 73815 lies at $P_{rot} = 31.1^{+1.3}_{-1.1}$ days and $t = 7.3 \pm 0.3$ Gyr (isochronal age), in agreement with the predictions of standard spin-down models.

diversity, particularly chemical composition, impacts these relations. Studies have shown that metallicity can influence both angular-momentum loss and the behavior of activity proxies (e.g., V. See et al. 2024; P. V. Souza dos Santos et al. 2024; G. Carvalho-Silva et al. 2025). As highlighted in recent discussions of stellar-activity evolution, a multidimensional perspective could be crucial for advancing gyrochronology and stellar rotational evolution studies.

Rotational modulation signals in light curves are typically most sensitive to starspots, which makes their detection particularly challenging in old Sun-like stars. Nevertheless, complementary ground-based observations are essential for advancing our understanding of stellar rotation. From the ground, stars of interest in both hemispheres can be monitored, free from the narrow geometric constraints of space-mission fields, thereby broadening the parameter space explored. In addition, high-precision spectroscopy with state-of-the-art instruments provides well-characterized diagnostics of stellar activity. While starspots are commonly used as proxies for magnetic fields (F. Menezes et al. 2024), other activity indicators are more sensitive to bright, long-lived regions such as faculae and plages. This enables stellar rotation to be traced through different manifestations of magnetic activity, providing valuable cross comparisons. Finally, it would be useful if old solar twins could be observed simultaneously with photometry and spectroscopy.

7. Conclusions

Our results demonstrate that ESPRESSO observations provide a high-fidelity detection of rotational modulation in an old

solar twin, adding a critical benchmark to the sparse sample of such stars with directly measured periods. The multi-dimensional GP analysis constrains the stellar rotation period of HIP 73815 to $P_{\rm rot} = 31.1^{+1.3}_{-1.1}$ days, consistent with the range of 30–32 days indicated by the most reliable activity proxies (RVs and bisector span). When combined with the observed color index ($B - V = 0.663 \pm 0.006$), gyrochronology relations yield an age of $t = 5.8 \pm 1.1$ Gyr, in excellent agreement with expectations for an old solar twin and reinforcing the reliability of the measured period.

This star therefore provides an important reference point for testing gyrochronology beyond the solar age, complementing the small but growing set of Sun-like stars with robust rotation periods. Further studies of rotation detection across different activity phases would clarify whether prior knowledge of the stellar magnetic cycle, and of the specific phase the star is currently in, could further enhance the interpretation of the observed inhomogeneities and help disentangle the relative contributions of spots and faculae, whose contrasting effects on line profiles produce distinct signatures in RVs and activity indicators. Clarifying the relative roles between active regions and activity indicators is key to interpreting the physical origin of the variability. Additionally, it would be particularly valuable if asteroseismic data were available for this star and for other similar solar twins, as such observations would provide excellent constraints on stellar rotation and internal structure, thereby improving our ability to interpret surface activity and its impact on angular-momentum evolution.

Acknowledgments

G.C.S. thanks the FAPESP PhD fellowships 2021/01303-3 and 2023/16319-8. J.M. thanks the support of FAPESP (2018/04055-8). R.D.H. is funded by the UK Science and Technology Facilities Council (STFC)'s Ernest Rutherford Fellowship (grant No. ST/V004735/1). This research has made use of the SIMBAD database, operated at CDS, Strasbourg, France.

Facility: ESO: ESO:3.6m, VLT:Antu, VLT:Kueyen.

Software: ACTIN (J. Gomes da Silva et al. 2018, 2021), Astropy (Astropy Collaboration et al. 2013, 2018, 2022), Astroquery (A. Ginsburg et al. 2019), Matplotlib (J. D. Hunter 2007), NumPy (C. R. Harris et al. 2020), pandas (W. McKinney 2010), pyaneti (O. Barragán et al. 2022), q2 (I. Ramírez et al. 2014).

ORCID iDs

G. Carvalho-Silva https://orcid.org/0000-0002-0715-709X
O. Barragán https://orcid.org/0000-0003-0563-0493
R. D. Haywood https://orcid.org/0000-0001-9140-3574
J. Meléndez https://orcid.org/0000-0002-4933-2239
S. A. Barnes https://orcid.org/0000-0001-7152-5726

References

Aigrain, S., Llama, J., Ceillier, T., et al. 2015, MNRAS, 450, 3211
Almeida-Fernandes, F., & Rocha-Pinto, H. J. 2018, MNRAS, 476, 184
Araújo, A., Lima, C., Menezes, F., & Valio, A. 2025, ApJL, 985, L28
Astropy Collaboration, Price-Whelan, A. M., Lim, P. L., et al. 2022, ApJ, 935, 167
Astropy Collaboration, Price-Whelan, A. M., Sipőcz, B. M., et al. 2018, AJ, 156, 123
Astropy Collaboration, Robitaille, T. P., Tollerud, E. J., et al. 2013, A&A, 558, A33
Barnes, S. A. 2003, ApJ, 586, 464
Barnes, S. A. 2007, ApJ, 669, 1167
Barnes, S. A., & Kim, Y.-C. 2010, ApJ, 721, 675
Barragán, O., Aigrain, S., Rajpaul, V. M., & Zicher, N. 2022, MNRAS, 509, 866
Barragán, O., Gandolfi, D., & Antoniciello, G. 2019, MNRAS, 482, 1017
Barragán, O., Gillen, E., Aigrain, S., et al. 2023, MNRAS, 522, 3458
Bazot, M., Ireland, M. J., Huber, D., et al. 2011, A&A, 526, L4
Carlos, M., Meléndez, J., Spina, L., et al. 2019, MNRAS, 485, 4052
Carvalho-Silva, G., Meléndez, J., Rathsam, A., et al. 2025, ApJL, 983, L31
Casali, G., Montalbán, J., Miglio, A., et al. 2025, MNRAS, 541, 2631
Chaplin, W. J., Cegla, H. M., Watson, C. A., Davies, G. R., & Ball, W. H. 2019, AJ, 157, 163
Christensen-Dalsgaard, J. 2021, LRSP, 18, 2
de Mello, G. F., & da Silva, L. 1997, ApJL, 482, L89
dos Santos, L. A., Meléndez, J., do Nascimento, J.-D., et al. 2016, A&A, 592, A156
Giles, H. A. C., Collier Cameron, A., & Haywood, R. D. 2017, MNRAS, 472, 1618
Ginsburg, A., Sipőcz, B. M., Brasseur, C. E., et al. 2019, AJ, 157, 98
Gomes da Silva, J., Figueira, P., Santos, N., & Faria, J. 2018, JOSS, 3, 667
Gomes da Silva, J., Santos, N. C., Adibekyan, V., et al. 2021, A&A, 646, A77
Gruner, D., Barnes, S. A., & Weingrill, J. 2023, A&A, 672, A159
Harris, C. R., Millman, K. J., van der Walt, S. J., et al. 2020, Natur, 585, 357
Haywood, R. D., Collier Cameron, A., Queloz, D., et al. 2014, MNRAS, 443, 2517
Haywood, R. D., Collier Cameron, A., Unruh, Y. C., et al. 2016, MNRAS, 457, 3637
Haywood, R. D., Milbourne, T. W., Saar, S. H., et al. 2022, ApJ, 935, 6
Hunter, J. D. 2007, CSE, 9, 90
Kawaler, S. D. 1988, ApJ, 333, 236
Kotorashvili, K., Blackman, E. G., & Owen, J. E. 2023, MNRAS, 522, 1583
Lockwood, G. W., Skiff, B. A., Henry, G. W., et al. 2007, ApJS, 171, 260
Lorenzo-Oliveira, D., Meléndez, J., Ponte, G., & Galarza, J. Y. 2020, MNRAS, 495, L61
Lorenzo-Oliveira, D., Meléndez, J., Yana Galarza, J., et al. 2019, MNRAS, 485, L68
Mamajek, E. E., & Hillenbrand, L. A. 2008, ApJ, 687, 1264
Martos, G., Meléndez, J., Rathsam, A., & Carvalho Silva, G. 2023, MNRAS, 522, 3217
Mayor, M., Pepe, F., Queloz, D., et al. 2003, Msngr, 114, 20
McKinney, W. 2010, in Proc. 9th Python in Science Conf., ed. S. van der Walt & J. Millman, 56
Meléndez, J., Ramírez, I., Karakas, A. I., et al. 2014, ApJ, 791, 14
Menezes, F., Araújo, A., & Valio, A. 2024, A&A, 691, L12
Mestel, L. 1968, MNRAS, 138, 359
Metcalfe, T. S., & Egeland, R. 2019, ApJ, 871, 39
Meunier, N., Desort, M., & Lagrange, A. M. 2010, A&A, 512, A39
Monroe, T. R., Meléndez, J., Ramírez, I., et al. 2013, ApJL, 774, L32
Nataf, D. M., Schlaufman, K. C., Reggiani, H., & Hahn, I. 2024, ApJ, 976, 87
Netto, Y., Lorenzo-Oliveira, D., Meléndez, J., et al. 2021, AJ, 162, 160
Nissen, P. E. 2015, A&A, 579, A52
Parker, E. N. 1958, ApJ, 128, 664
Pepe, F., Cristiani, S., Rebolo, R., et al. 2021, A&A, 645, A96
Ponte, G., Lorenzo-Oliveira, D., Melendez, J., Yana Galarza, J., & Valio, A. 2023, MNRAS, 522, 2675
Queloz, D., Bouchy, F., Moutou, C., et al. 2009, A&A, 506, 303
Rajpaul, V., Aigrain, S., Osborne, M. A., Reece, S., & Roberts, S. 2015, MNRAS, 452, 2269
Ramírez, I., Meléndez, J., Bean, J., et al. 2014, A&A, 572, A48
Ramírez, I., Michel, R., Sefako, R., et al. 2012, ApJ, 752, 5
Rasmussen, C. E., & Williams, C. K. I. 2005, Gaussian Processes for Machine Learning (The MIT Press)
Rauer, H., Catala, C., Aerts, C., et al. 2014, ExA, 38, 249
Saunders, N., van Saders, J. L., Lyttle, A. J., et al. 2024, ApJ, 962, 138
See, V., Lu, Y. L., Amard, L., & Roquette, J. 2024, MNRAS, 533, 1290
Shejeelammal, J., Meléndez, J., Rathsam, A., & Martos, G. 2024, A&A, 690, A107
Skumanich, A. 1972, ApJ, 171, 565
Soderblom, D. R. 2010, ARA&A, 48, 581
Souza dos Santos, P. V., Porto de Mello, G. F., Costa-Bhering, E., et al. 2024, MNRAS, 532, 563
Spina, L., Meléndez, J., Karakas, A. I., et al. 2018, MNRAS, 474, 2580
Swastik, C., Banyal, R. K., Narang, M., Unni, A., & Sivarani, T. 2024, AJ, 167, 270
Thompson, S. J., Queloz, D., Baraffe, I., et al. 2016, SPIE, 9908, 99086F
Tuchow, N. W., Stark, C. C., & Mamajek, E. 2024, AJ, 167, 139
van Saders, J. L., Ceillier, T., Metcalfe, T. S., et al. 2016, Natur, 529, 181
van Saders, J. L., Pinsonneault, M. H., & Barbieri, M. 2019, ApJ, 872, 128
Veyette, M. J., & Muirhead, P. S. 2018, ApJ, 863, 166